AIAA Journal
Vol. 57, No. 1, January 2019

Parametric Modal Decomposition of Dynamic Stall

Dustin G. Coleman*
Cornerstone Research Group, Inc., Miamisburg, Ohio 45342
and
Flint O. Thomas,† Stanislav Gordeyev,‡ and Thomas C. Corke§
University of Notre Dame, Notre Dame, Indiana 46556

DOI: 10.2514/1.J057077

The chordwise, unsteady pressure difference field for harmonically oscillating airfoils operating in the attached flow, light dynamic stall, and deep dynamic stall regimes has been modally decomposed to identify well-defined modal structures that persist across a vast parameter space of pitching parameters (i.e., reduced frequency, mean angle of attack, and oscillation amplitude). The pressure difference fields were acquired at a chord Reynolds number and Mach number of $Re_c = 1.12 \times 10^6$ and $M_\infty = 0.2$, respectively, demonstrating results applicable to rotorcraft flight conditions. Notably, only four mode shapes were required to reconstruct the aerodynamic loads anywhere within the parameter space. Likewise, the same mode shapes showed a remarkable ability to reconstruct the aerodynamic loads of other (non-native) airfoil geometries with a similar precision. The parametric modal decomposition outlined provides a foundation to elucidate the physics of the dynamic stall phenomenon as well as reduced-order modeling techniques for the aerodynamic loading.

Nomenclature

C_m = quarter-chord pitching moment coefficient
C_n = normal force coefficient
C_p = pressure coefficient
c = chord length, m
d = modal coefficient
f = pitching frequency, Hz
k = reduced frequency; $2\pi fc/U_\infty$
M = Mach number
p = pressure, mbar
Re_c = chord-based Reynolds number; cU_∞/ν
RMP = relative magnitude parameter
s = span, m
T = oscillation period, s
t = time, s
U = mean velocity, m/s
u = fluctuating velocity, m/s
x = dimensional chordwise coordinate, m
$\dot{\alpha}$ = pitch rate, deg/s
α = angle of attack, deg
α_0 = mean angle of attack, deg
α_1 = oscillation amplitude, deg
γ = specific heat ratio
η = correlation value
λ = eigenvalue
ξ = nondimensional chordwise coordinate; x/c
ψ = mode shape

Subscripts

airfoil = on airfoil surface
i, j, n = index counter
inv = calculated inviscid value
rms = root-mean-square value
sp = stall penetration
ss = static stall value
steady = steady flow condition value
unsteady = unsteady flow condition value
∞ = freestream

Superscripts

l = on airfoil lower surface
u = on airfoil upper surface
$*$ = fluctuation with respect to steady, viscous value
= spatially integrated value

I. Introduction

WITH its long-standing influence on the rotorcraft, wind energy, and turbomachinery communities, the problem of dynamic stall continues to cultivate new investigations concerning the physical mechanisms underlying the process. These are motivated by attempts to better understand, model, and control its aerodynamic influence on airfoils. This flow phenomenon is characterized as the unsteady separation evolution in which stall is delayed as a lifting surface rapidly exceeds its static stall angle of attack. Associated with such a motion trajectory are the initiation, growth, detachment, and convection of a large, coherent, vortical structure that forms near the airfoil leading edge that is known as the dynamic stall vortex. The emergence of this flow structure introduces large fluctuations in the pressure field and consequently develops nonlinear aerodynamic loadings, exhibiting large excursions with respect to typical static aerodynamic behavior. These nonlinear aerodynamics often result in impulsive loading of the mechanical system, leading to the excitation of aeroelastic instabilities and reduced fatigue life of critical components [1].

Despite being the topic of an extensive body of research spanning the past six decades, the dynamic stall process remains to be fully understood and accurately predicted for arbitrary airfoil motions and geometries. Ericsson and Reding [2] stated that, "only if the unsteady stall mechanism is understood can an 'analytic extrapolation' to full scale [rotors] be made with confidence," conveying the importance and difficulty of predicting the unsteady process. Historically, theoretical modeling of unsteady aerodynamics is limited to attached flow cases such as the classical solutions contributed by Theodorsen [3], Wagner [4], and von Kármán and Sears [5]. Because of the difficulties found in accurately and consistently predicting the stall process, engineering efforts for the design of advanced airfoil

Received 29 December 2017; revision received 26 June 2018; accepted for publication 5 September 2018; published online 24 November 2018.

*Research Engineer, Aerospace Systems. Member AIAA.
†Professor, Aerospace and Mechanical Engineering, Institute for Flow Physics and Control. Associate Fellow AIAA.
‡Associate Professor, Aerospace and Mechanical Engineering, Institute for Flow Physics and Control. Associate Fellow AIAA.
§Clark Chair Professor, Aerospace and Mechanical Engineering, Institute for Flow Physics and Control. AIAA Fellow.

sections rely heavily on experimentally driven, semi-empirical models. Examples include the Leishman–Beddoes [6], the ONERA [7], and the Goman–Khrabrov [8,9] models, which have system coefficients and time-delay parameters that are tuned by regression fitting with experimental results for steady and dynamic pitching of the airfoil under investigation. These models have proven to be computationally faster and less expensive than full computational-fluid-dynamics simulations [10]. However, they require the experimental data that are being predicted, or at the very least, minimal unsteady testing for all airfoils considered. In this sense, the models are "postdictive" in nature. To continue the advancement of rotor blade technology, it is desirable to have a dynamic stall model that is computationally robust and requires few input parameters to describe the airloads for the geometry under consideration. Additionally, it is important in model development to distinguish between generic aspects of the dynamic stall process and those that are geometry specific.

In light of these shortcomings, this paper will demonstrate a modal decomposition of an airfoil surface pressure field that results in a robust low-order representation of the dynamic stall phenomenon in terms of the pressure response on the airfoil surface, providing the foundation for an efficient reduced-order model. The model basis is developed using parametric modal decomposition (PMD) [11,12], which not only allows the unsteady surface pressure field of an airfoil to be accurately reconstructed but also provides a framework for additional in-depth analysis of the dynamic stall phenomenon using sparse data-based machine learning techniques to extract parsimonious, nonlinear dynamical system representations [13–16].

The remainder of this paper is organized as follows. Section II presents the formulation for the parametric modal decomposition. The experimental setup is found in Sec. III. Results for the modal decomposition are found in Sec. IV. And Sec. V discusses the conclusions drawn from the results with suggestions for future work.

II. Parametric Modal Decomposition

Parametric modal decomposition (PMD) expresses a multidimensional function in modal form where the leading coefficients contain the parameter space dynamics, and the mode shapes form an optimum reduced basis, from which the dynamical system may be reconstructed with the least amount of modes compared to any other basis. Consider the cycle-averaged pressure on an airfoil, $p(\xi, \alpha; k, \alpha_0, \alpha_1)$, where $\xi = x/c$ is the nondimensional chordwise location, α is the angle of attack, $k = \pi f c / U_\infty$ is the reduced frequency (a ratio of convective to imposed pitch motion time-scales), α_0 is the mean angle of attack, and α_1 is the amplitude of the cyclic pitch motion. The pressure field is expressed in terms of an expansion of purely spatial orthonormal modes $\psi_i(\xi)$ that provide an optimal representation of the pressure field over the given parameter space,

$$p(\xi, \alpha; k, \alpha_0, \alpha_1) = \sum_i d_i(\alpha; k, \alpha_0, \alpha_1)\psi_i(\xi), \qquad \|\psi_i\|^2 = 1 \quad (1)$$

The modes are optimum in the sense that they reconstruct the pressure field with the minimal number of modes. The dynamics of the pressure field within the parameter space is embodied in the modal coefficients d_i. The coefficients are obtained from the orthogonality condition of the spatial modes,

$$d_i(\alpha; k, \alpha_0, \alpha_1) = \int_{\Omega_\xi} (p(\xi, \alpha; k, \alpha_0, \alpha_1) \cdot \psi_i(\xi))\, \mathrm{d}\xi \qquad (2)$$

where Ω_ξ represents the domain $\xi \in [0, 1]$.

The spatial modes are obtained from solving the following integral eigenvalue problem

$$\int_{\Omega_\xi} \langle p(\xi, \alpha; k, \alpha_0, \alpha_1) \cdot p(\xi', \alpha; k, \alpha_0, \alpha_1)\rangle \psi(\xi')\, \mathrm{d}\xi' = \lambda\psi(\xi) \quad (3)$$

where $\langle p(\xi, \alpha; k, \alpha_0, \alpha_1) \cdot p(\xi', \alpha; k, \alpha_0, \alpha_1)\rangle = R(\xi, \xi')$ is the autocorrelation function, averaged over the parametric space $(\alpha, k, \alpha_0, \alpha_1)$, of $p(\xi, \alpha; k, \alpha_0, \alpha_1)$ and λ is the corresponding eigenvalue [17]. Modes are prioritized according to their relative energy E_R by comparing respective eigenvalues, where $E_R = \lambda_i / \sum_j \lambda_j$.

This technique is similar to proper orthogonal decomposition (POD), where a spatiotemporal data set is spectrally decomposed into time varying coefficients and spatial mode shapes. However, PMD differs from POD in that the modal coefficients carry information concerning the entirety of a multidimensional parameter space and may be viewed with respect to any given parameter whereas POD is usually applied to a signal at a fixed point in the parameter space. For example, previous applications of POD to dynamic stall investigations [18–20] have focused on the reduction of velocity field measurements, obtained using particle image velocimetry (PIV), to identify flow features associated with the phenomenon at a fixed parameter space location (i.e., fixed Mach number, mean angle of attack, oscillation amplitude, and frequency). In contrast to conventional POD, the PMD approach provides modes that are globally optimized across the full parameter space $(\alpha, k, \alpha_0, \alpha_1)$ of the reported experiments.

III. Experimental Setup

All experiments were performed in the Mach 0.6 closed-return wind tunnel located at the University of Notre Dame. A top-down schematic view of the wind tunnel is shown in Fig. 1 along with many of its key features. The flow is driven by a 1.3 MW (1750 hp) variable-rotation-frequency ac motor that turns a 2.44-m-diam (8-ft-diam), high-solidity, two-stage fan. At a given flow speed, equilibrium temperature is achieved by actively cooling the turning vanes downstream of the fan via 4.44°C (40°F) water. The flow is then conditioned by a 12.7-cm-thick (5-in.-thick) honeycomb wall of 0.635 cm (0.25 in.) nominal diameter followed by five #28 wire

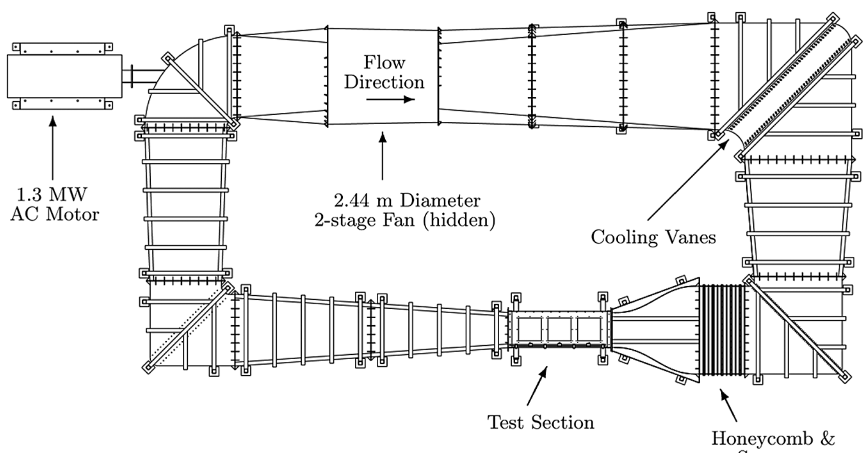

Fig. 1 University of Notre Dame Mach 0.6 wind tunnel, top view.

screens leading to a 6 : 1 inlet contraction. The resulting freestream turbulence intensity level of the empty tunnel is $u_{\mathrm{rms}}/U_{\infty} \approx 0.05\%$.

The tunnel has three interchangeable test sections, of which one has been retrofitted to accommodate unsteady, pitching airfoil experiments. This test section is depicted in Fig. 2 along with the pitching mechanism. A more detailed description of the test section internal structure is shown in Fig. 3. Airfoil models are mounted between two 1.905-cm-thick (0.75-in.-thick) aluminum splitter plates having elliptical leading edges and tapered trailing edges. The airfoil models are fixed to oscillate about their quarter-chord position.

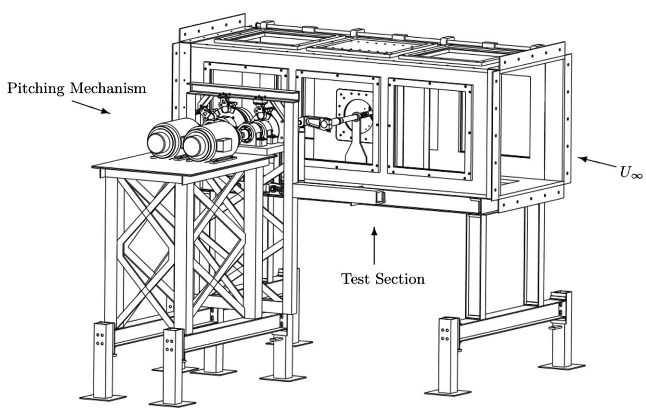

Fig. 2 Dynamic stall test section and pitching mechanism.

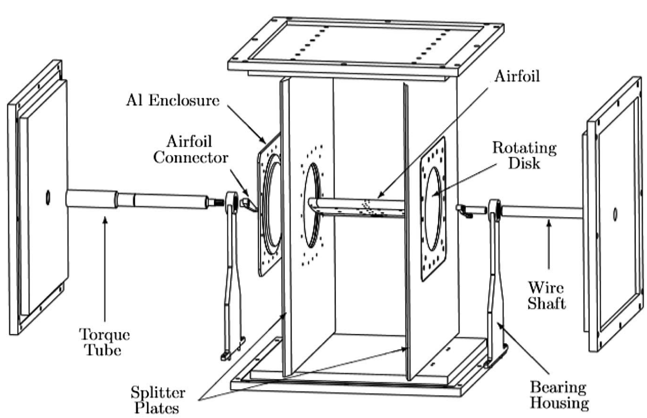

Fig. 3 Test section internal pitching structure.

Table 1 Airfoil characteristics

Airfoil	Leading-edge radius, %c	Thickness, %c	Camber, %c	Leading-edge mode	α_{ss}, deg
NACA 23012	1.581	12.00	1.8	— —	14.3
PA1	0.589	9.98	1.9	Tripped	13.0
PA2	0.987	11.43	2.2	Tripped	13.2

Each side of an airfoil model is fitted with a 1.27-cm-thick (0.5-in.-thick) Lexan end plate (rotating disk), which is housed inside the splitter plate and secured with an aluminum enclosure, creating a labyrinth seal. Instrumentation cables are carried out of the test section opposite the pitching mechanism, whereas the pitching motion is driven through a drive shaft, connected to the mechanism. The drive shaft and wire shaft are both supported by passing through ball bearings housed in aluminum casings that are secured to the test section floor and located just outside of each splitter plate. The bearing houses facilitate the transmission of aerodynamic loads to the test section.

The pitching mechanism, constructed in partnership with Bell Helicopter, is a unique dual-input walking beam design that allows two-degree-of-freedom motion to be prescribed on the airfoil test article. A detailed, labeled view of the pitching mechanism is shown in Fig. 4. The adjustable pitch link is used to control the mean angle of attack α_0 by varying its length. Oscillation amplitude, provided by each flywheel input, is controlled by offsetting the respective spindle placement from the center using the Acme threads. The walking beam acts as a mechanical adder of the two frequency and amplitude inputs from the two flywheels, to produce complex pitching trajectories at the torque tube connection. Each flywheel is driven by a Marathon 7.457 kW (10 hp) Black Magic 420 VAC motor. Dynapar internal encoders monitored by Yaskawa F-7 drives provide rotation-frequency control independently for each motor. For the purposes of this experiment, only single-frequency pitching motions were considered. To achieve a single-frequency output, brakes are applied to the second flywheel (right), and only the first motor (left) is driven.

A. Airfoil Models

Three different airfoil test articles were used throughout the course of the experiments. The considered geometries are a NACA 23012 and two custom designs denoted PA1 and PA2. Details regarding the essential geometric characteristics of the airfoils are provided in Table 1. Each airfoil model was constructed from three high-strength aluminum (Al 7075-t6) pieces as shown in Fig. 5. This design facilitated the proper installation of flush-mounted unsteady pressure transducers and safe internal storage of transducer cables while maintaining a rigid housing with hydrodynamically smooth surfaces. To lower the inertial loading, improve the stability of the system, and

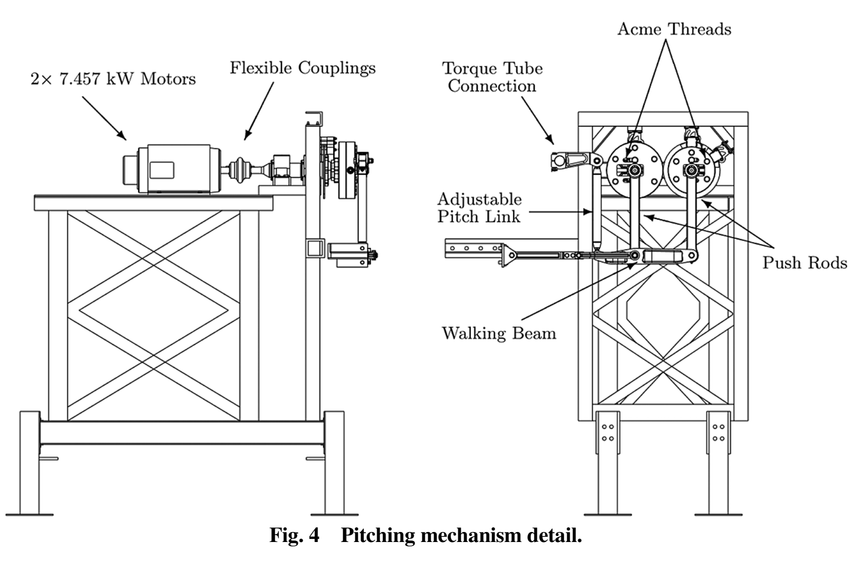

Fig. 4 Pitching mechanism detail.

provide wire paths, two large spanwise sections were removed from the internal mass. Each model chord length was set at $c = 0.254$ m (10 in.) and had a span of $s = 0.3556$ m (14 in.) to operate within the test section splitter plates as previously described. These dimensions result in a maximum blockage of ≤5% at the maximum angles of attack encountered in the experiments, making their effect negligible. The NACA 23012 model is depicted in Fig. 6, showing the spanwise cutouts, wire storage, and instrumentation installation. A similar approach was used for the construction of the other airfoil models.

B. Instrumentation

1. Surface Pressure

Unsteady surface pressure was measured along the midspan of each airfoil model using 31–33 high-frequency response, absolute pressure transducers manufactured by Kulite and Endevco as shown in Table 2. The measurable pressure range for the Kulite transducers was 0–1723 mbar (0–25 psia) with a frequency response up to 240 kHz. Likewise, the Endevco transducers exhibited a pressure range of 0–1034 mbar (0–15 psia) with a frequency response up to 180 kHz. The transducers were positioned along the chord using a cosine distribution described as

$$\xi_n = 1 - \cos\left(\frac{n\pi}{2N}\right) \tag{4}$$

where $N = 16$, $n = 0, 1, \ldots, N-1$, and ξ_n is the nondimensional chord station of the pressure transducer ($N = 15$ on the NACA 23012). The last pressure port was located at $\xi_{16} = 0.981$ ($\xi_{15} = 0.975$ on the NACA 23012) due to both the finite thickness of the sensor and the sharp trailing edge of the airfoil geometries.

2. Freestream Pressure

The freestream static and total pressure are measured approximately 1 m (3.28 ft) upstream of the center of the splitter plate assembly via a pitot static probe. Each output of the probe is connected to an independent Setra model 270 high-accuracy, absolute, barometric pressure transducer. The Setra model 270 transducers used have an accuracy of ±0.03% Full Scale (FS) with a 0.027% FS linearity. The measurable pressure range is 600–1100 mbar (8.70–15.95 psi).

3. Angle of Attack

The instantaneous angle of attack was monitored by connecting the wire shaft (Fig. 3) to a Positek RIPS P500 inductive rotary sensor, fixed to the tunnel outer window. The sensor has a linear output of 0–5 V over the range 0–60 deg. The output has a frequency response greater than 10 kHz and a noise level less than 0.02% Full Scale Output (FSO).

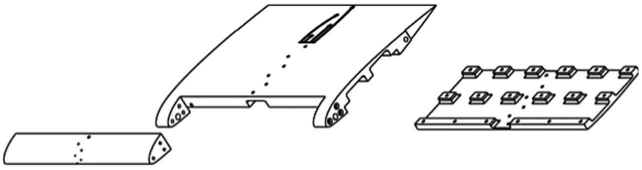

Fig. 5 Three-piece airfoil construction.

Table 2 Pressure transducer details

Chord station		Pressure sensor		
Number	x_n/c	Manufacturer	Type	Diameter, mm (in.)
0	0.0000	Kulite	XCL-062-25A	1.60 (0.066)
1[a]	0.0030	Kulite	XCL-062-25A	1.60 (0.066)
2	0.0055	Kulite	XCL-062-25A	1.60 (0.066)
3	0.0219	Kulite	XCL-062-25A	1.60 (0.066)
4	0.0489	Kulite	XCL-093-25A	2.40 (0.095)
5	0.0865	Kulite	XCL-093-25A	2.40 (0.095)
6	0.1340	Kulite	XCL-152-25A	3.80 (0.152)
7	0.1910	Kulite	XCL-152-25A	3.80 (0.152)
8	0.2569	Kulite	XCL-152-25A	3.80 (0.152)
9	0.3309	Kulite	XCL-152-25A	3.80 (0.152)
10	0.4122	Kulite	XCL-152-25A	3.80 (0.152)
11	0.5000	Kulite	XCL-152-25A	3.80 (0.152)
12	0.5933	Kulite	XCL-152-25A	3.80 (0.152)
13	0.6910	Endevco	8515C-15	6.35 (0.250)
14	0.7921	Endevco	8515C-15	6.35 (0.250)
15	0.8955	Endevco	8515C-15	6.35 (0.250)
16	0.9810	Endevco	8515C-15	6.35 (0.250)

[a]Not on the NACA 23012.

C. Data Acquisition

The analog pressure signals were low-pass, anti-alias filtered at 2.5 kHz before being amplified and DC offset to provide the highest signal-to-noise ratio possible. All pressure (freestream and surface) and angle-of-attack signals were then simultaneously digitized at a sampling frequency of $f_s = 5$ kHz by a Microstar Laboratories DAP5380a and three MSXB 028 simultaneous sampling boards, which offer 12-bit resolution. The digitized time-series data were then stored for post-processing.

IV. Results

Experiments were performed on each of the airfoils listed in Table 1 in a parameter space that encompassed unsteady attached flow, light stall, and deep stall regimes at $M_\infty = 0.2$ and $Re_c = 1.12 \times 10^6$. In each case, the surface pressure field was decomposed using PMD with the objective of discerning both common and disparate features of dynamic stall across the full parameter space. Throughout this analysis the aerodynamic loads are considered as a compliment assisting in the physical interpretation of PMD mode shapes. The two loads used are the normal force and the quarter-chord pitching moment described in a nondimensional form as

$$C_n = \int_0^1 (C_p^l - C_p^u)\,\mathrm{d}\xi \tag{5}$$

$$C_m = \int_0^1 ((C_p^l - C_p^u) \cdot (0.25 - \xi))\,\mathrm{d}\xi \tag{6}$$

respectively, where the superscripts indicate the lower (l) and upper (u) surfaces of the airfoil. The pressure coefficient C_p is defined as

$$C_p = \frac{2}{\gamma M_\infty^2}\left(\frac{P_{s,\mathrm{air\,foil}}}{P_\infty} - 1\right) \tag{7}$$

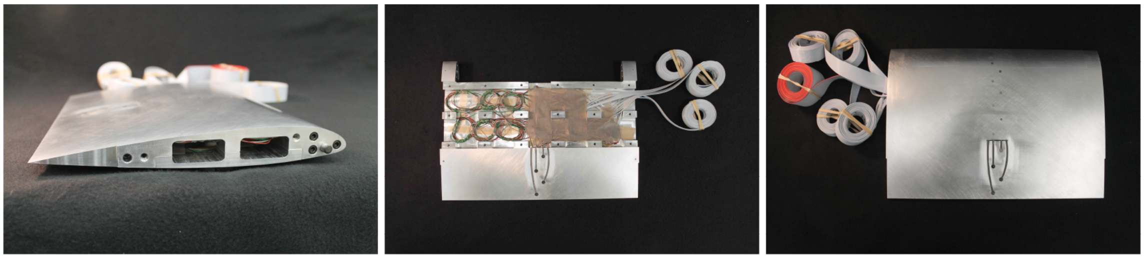

a) Side view b) Instrumentation c) Top view

Fig. 6 NACA 23012 model.

where γ is the specific heat ratio, M_∞ is the freestream Mach number, $P_{s,\text{air foil}}$ is the airfoil surface pressure, and P_∞ is the freestream static pressure. A modal contribution to the aerodynamic loads will be defined in Sec. IV.B.

A. Change of Reference Frame

A change in reference frame is first applied to view the unsteady surface pressure field over the pitching airfoil as a perturbation to the steady, attached flow pressure field. That is, the steady, viscous pressure field, obtained from static measurements, is removed from the experimental dataset. Here, steady refers to a collection of static measurements taken at multiple angles of attack.

To assess the validity of the steady experimental results, the C_n values from two previous experiments involving a NACA 23012 produced by NACA [21] (open squares) and Leishman [22] (crosses) are also displayed in Fig. 7. The Reynolds number of the current experiment is $Re_c = 1.12 \times 10^6$. Similarly for the NACA and Leishman experiments, this value was $Re_c = 1.6 \times 10^6$. Here, excellent agreement is realized in the normal force coefficient slope $\partial C_n/\partial\alpha$, for all three experiments, and the stall angle of the current experiment matches that realized in Leishman's work.

The pressure field calculated from a static Smith–Hess panel method (corrected for viscous effects via static experimental results in the fully attached flow regime) is removed from the experimentally acquired unsteady pressure fields, leaving the unsteady surface pressure coefficients defined as

$$C_p^*(\xi, \alpha, \dot{\alpha}) \equiv C_p(\xi, \alpha, \dot{\alpha}) - C_{p,\text{static}}(\xi, \alpha) \tag{8}$$

By moving to this reference frame, the PMD analysis produces spatial modes of the C_p^* field that represent, by definition, perturbations from the static, attached flow pressure field. As such, this field will account for both separation and unsteady effects.

The process of changing the reference frame has been illustrated using the NACA 23012 airfoil due to the large body of literature that supports the current experimental results, which is not available for the custom airfoils used in this work. However, it should be noted that moving to this frame is a generic procedure that can be calculated for any arbitrarily chosen airfoil geometry.

B. ψ-Mode Calculation

This section presents the application of PMD to the PA2 airfoil. Table 3 provides the pitch motion parameters used for each experiment involving the PA2 geometry. Here, the pitching amplitude and the freestream Mach number have been fixed at $\alpha_1 = 8$ deg and $M_\infty = 0.2$, respectively. This corresponds to a chord Reynolds number of $Re_c = 1.12 \times 10^6$. Likewise, each experiment listed in Table 3 consists of ~100 pitching cycles, which has been demonstrated to be adequate for achieving stationary statistics [23]. The resulting

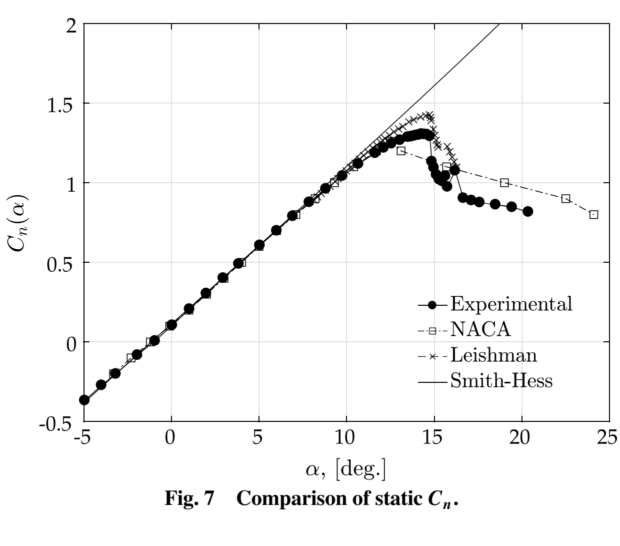

Fig. 7 Comparison of static C_n.

Table 3 PA2 parameter cases ($\alpha_1 = 8$ deg, $M_\infty = 0.2$, $U_\infty \approx 70$ m/s, $Re_c = 1.12 \times 10^6$)

Case number	α_0, deg	k	Type
1	7	0.020	AF
2	7	0.050	AF
3	7	0.075	AF
4	8	0.020	LS
5	8	0.050	LS
6	8	0.075	LS
7	9	0.020	LS
8	9	0.050	LS
9	9	0.075	LS
10	10	0.020	LS
11	10	0.050	LS
12	10	0.075	LS
13	11	0.020	LS
14	11	0.050	LS
15	11	0.075	LS
16	12	0.020	DS
17	12	0.050	DS
18	12	0.075	DS
19	13	0.020	DS
20	13	0.050	DS
21	13	0.075	DS
22	14	0.020	DS
23	14	0.050	DS
24	14	0.075	DS
25	15	0.020	DS
26	15	0.050	DS
27	15	0.075	DS

flow regime produced for each experiment is designated in Table 3 as attached flow pitching (AF), light stall (LS), and deep stall (DS). Because the aerodynamic loads during attached flow pitching are well understood from analytical techniques [3–5], the cases here are weighted based on the number of experiments in the LS and DS regimes where leading-edge vortices and large, unsteady pressure fluctuations exist.

Typically, low-order models of dynamic stall focus on reconstructing the aerodynamic loads for a given pitching trajectory [24]. For this reason, it is advantageous to consider the pressure difference field associated with the calculation of the aerodynamic loads, that is, $\Delta C_p^*(\xi,\alpha,\dot{\alpha};k,\alpha_0) \equiv C_p^{l*}(\xi,\alpha,\dot{\alpha};k,\alpha_0) - C_p^{u*}(\xi,\alpha,\dot{\alpha};k,\alpha_0)$. This pressure difference field is the kernel of the integration defining both the normal force loading and the quarter-chord pitching moment as defined in Eqs. (5) and (6), respectively. Using this pressure field should produce a more rapidly converging reconstruction of the aerodynamic loads compared to the decomposition of the full pressure field C_p^* as discussed by McCroskey [25].

The pressure difference field ΔC_p^* collection assembled from the experiments in Table 3 is decomposed into parameter-independent, purely spatial, orthogonal ψ modes [$\psi = \psi(\xi)$] as was demonstrated for the surface pressure field in Eq. (1). Each ψ mode contributes to the aerodynamic loads as

$$C^*_{\underset{\text{PMD}}{n,i}}(\alpha, \dot{\alpha}) = d_i(\alpha, \dot{\alpha}) \underbrace{\int_0^1 \psi_i(\xi)\, \mathrm{d}\xi}_{C^\#_{n,i}} \tag{9}$$

$$C^*_{\underset{\text{PMD}}{m,i}}(\alpha, \dot{\alpha}) = d_i(\alpha, \dot{\alpha}) \underbrace{\int_0^1 (\psi_i(\xi) \cdot (0.25 - \xi))\, \mathrm{d}\xi}_{C^\#_{m,i}} \tag{10}$$

Here, $C^\#_{n,i}$ and $C^\#_{m,i}$ are the spatially integrated normal force and quarter-chord moment contributions, respectively. Notice that these values are constants regardless of the position within the parameter space. The magnitude of each modal contribution to the total aerodynamic loads is then the modal coefficient d_i modulated by the spatially integrated value, $C^\#_{n,i}$ or $C^\#_{m,i}$. Although the ΔC_p^* modes are ordered by their respective eigenvalues, λ_i (i.e., the scale of the modal

Table 4 PMD eigenvalues and aerodynamic load contribution parameters

Parameter	ψ_1	ψ_2	ψ_3	ψ_4	ψ_5
C_n RMP, %	97.48	2.19	0.12	0.17	0.02
Order [j]	1	2	4	3	5
C_m RMP, %	90.69	7.11	0.97	0.96	0.16
Order [j]	1	2	3	4	5

coefficients d_i), the modal contributions to the aerodynamic loads may rearrange their order of significance due to the imposed modulation of the integrated mode shapes. To demonstrate, consider the relative magnitude percentage (RMP), defined as

$$\mathrm{RMP} = \frac{\lambda_i \cdot |C^{\#}_{x,i}|}{\sum_j \lambda_j \cdot |C^{\#}_{x,j}|} \times 100\% \tag{11}$$

and the suggested ψ_i-mode ordering based on the respective RMP values. The j ordering tells where the ith mode should be due to the modulated eigenvalue magnitude as shown in Table 4.

Table 4 shows a very rapid convergence for each aerodynamic load with greater than 99% of the signal energy (calculated as the cumulative RMP) represented in just the first two and first four modes for C_n^* and C_m^*, respectively. In fact, retaining only the first two modes yields an RMP of 99.7% for C_n^* and 97.8% for C_m^*. Based on the RMP, only two modes are rearranged from the PMD eigenvalue ordering when considering the normal force reconstruction and none are with the quarter-chord moment.

Figure 8 uses the modal eigenvalue i ordering to show the first four ψ mode shapes, modal coefficients, and modal aerodynamic load contributions. In each subfigure of the modal coefficients and aerodynamic loads, three cases representing attached flow pitching ($\alpha_0 = 6.7$ deg, $k = 0.020$), light stall ($\alpha_0 = 9.7$ deg, $k = 0.050$), and deep stall ($\alpha_0 = 13.9$ deg, $k = 0.078$) are depicted as functions of nondimensional time t/T, where T is the airfoil oscillation period.

Examining the aerodynamic load coefficients C_n^* and C_m^*, it is quite remarkable that the first two modes ψ_1 and ψ_2 appear to be the sole significant contributors to both loads for all pitching regimes (i.e., attached flow pitching, light stall, and deep stall). Also, the third and fourth modes ψ_3 and ψ_4 supply additional information for the quarter-chord moment reconstruction but appear to be of minimal contribution to the normal force. This result suggests that the

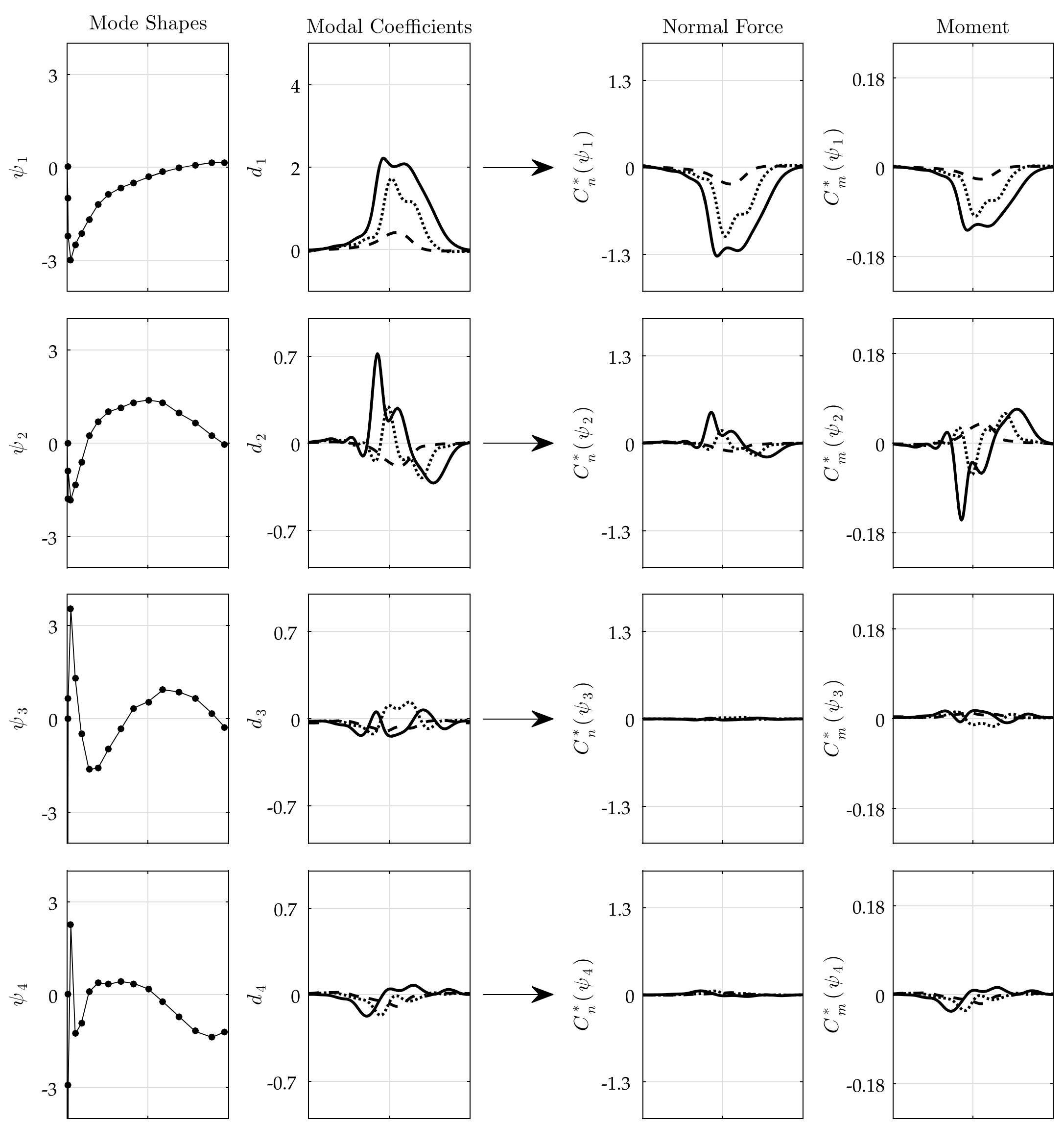

Fig. 8 PA2 ΔC_p^* ψ-mode load contributions: attached flow, $\alpha_0 = 6.7$ deg, $k = 0.020$ (dashed line); light stall, $\alpha_0 = 9.7$ deg, $k = 0.050$ (dotted line); and deep stall, $\alpha_0 = 13.9$ deg, $k = 0.078$ (solid line).

dynamic stall phenomenon, as viewed from the pressure difference field, can primarily be decomposed into two linearly independent contributing factors, which has obvious benefits in obtaining a low-order dynamic stall model.

The first mode ψ_1 appears to describe the loss of suction pressure in the leading-edge region during airfoil pitch-up. Based on the growth of the modal coefficient d_1 during pitch-up ($t/T = 0 \rightarrow 0.5$) and decay during pitch-down ($t/T = 0.5 \rightarrow 1.0$), it is clear that the suction pressure in the near leading-edge region (as a perturbation of the calculated attached flow value) is severely degraded as the angle of attack increases in incidence. The idea of suction pressure loss is further supported by the contributions of ψ_1 to the normal force and quarter-chord pitching moment, where each decreases to a large negative value as the angle of attack rises. In a similar manner, on the airfoil pitch-down ($t/T > 0.5$), mode 1 describes a more gradual reestablishment of leading-edge suction as both $C_n^*(t/T; \psi_1)$ and $C_m^*(t/T; \psi_1)$ increase from large negative values and approach zero at the end of the cycle.

The second mode shape ψ_2 exhibits a large suction pressure loading that peaks in the vicinity of the midchord and, therefore, is likely responsible for describing the pressure difference response due to the presence of the aft-propagating dynamic stall vortex. Supporting this claim, the modal coefficients d_2 for both the light and deep stall cases show a similar functional form, whereas the attached flow pitching trajectory (a case where no vortex is expected to exist) is fundamentally different. Likewise, evidence of the dynamic stall vortex is generally realized by the introduction of large fluctuations in the quarter-chord pitching moment due to the vortex's aftward propagation over the airfoil. These fluctuations are seen in the quarter-chord pitching moment contributions $C_m^*(t/T; \psi_2)$ for light stall and deep stall and not for attached flow pitching, which again suggests that ψ_2 is associated with the dynamic stall vortex. The ψ_2 mode serves to generate a large nose-down pitching moment perturbation as evidenced by $C_m^*(t/T; \psi_2)$ that coincides with augmentation of the normal force as evidenced by $C_n^*(t/T; \psi_2)$. This impulsive negative pitching moment is the primary source of high control loads limiting operational performance and contributes to airframe vibration, which reduces fatigue life of major components during the retreating blade stall event on helicopter rotors.

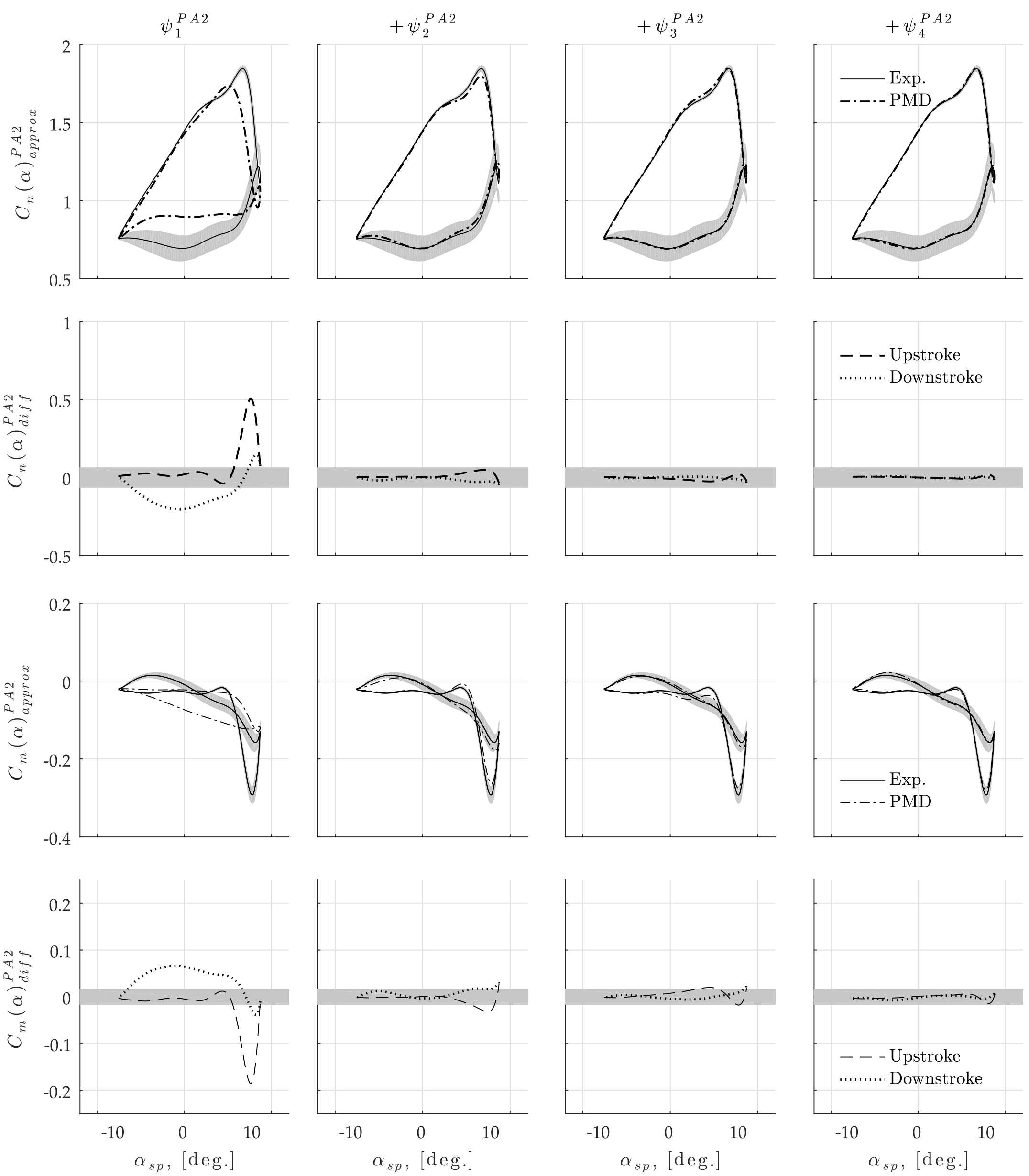

Fig. 9 PA2 deep stall aerodynamic load reconstruction. Label definition in text. Approximation plots: phase-averaged experimental data (solid line), standard deviation (shaded area). Difference plots: ±5% maximum amplitude (shaded area).

C. Aerodynamic Load Reconstruction

To demonstrate the efficiency of the PMD in capturing the unsteady aerodynamics across the parameter space, aerodynamic load reconstructions are considered using the mode shapes showing the largest contributions (i.e., ψ_1, ψ_2, ψ_3, and ψ_4). As an example, Figs. 9 and 10 depict the reconstructions of the normal force (top) and quarter-chord pitching moment (bottom) for a deep stall case ($\alpha_0 = 13.9$ deg, $k = 0.078$) and light stall case ($\alpha_0 = 9.7$ deg, $k = 0.050$), respectively. Note that these loads are the full representation with the calculated static attached flow component [$C_{p,\text{static}}(\xi, \alpha)$ in Eq. (8)] included. The rows labeled $C_x(\alpha)_{\text{approx}}$ show the phase-averaged experimental data as a solid line with the shaded area representing experimental standard deviation while the PMD approximation is shown as a dash-dotted line. Likewise, $C_x(\alpha)_{\text{diff}}$ gives the difference between the phase-averaged experimental values and the PMD approximation to investigate which parts of the trajectory have deficiencies. The upstroke motion is a dashed line, the downstroke motion is a dotted line, and the shaded region represents $\pm 5\%$ of the load maximum amplitude ($C_x^*|_{\max} - C_x^*|_{\min}$). The abscissa of each subfigure represents the values of stall penetration angle of attack $\alpha_{\text{sp}} = \alpha - \alpha_{\text{ss}}$, where α_{ss} is the static stall angle of attack.

The one mode approximation using ψ_1 captures the overall shape of each load trajectory. In Fig. 9, the lift slope change that occurs toward the top of the pitch trajectory that has typically been associated with the existence of the dynamic stall vortex is not captured with just ψ_1. Likewise, the sharp nose down pitching moment associated with the aft advection of the dynamic stall vortex is not realized. This behavior corroborates the mode shape analysis in Sec. IV.B that suggested ψ_1 accounts primarily for the leading-edge suction pressure loss.

Adding ψ_2 to the approximations results in a nearly exact reconstruction of the normal force for both the deep and light stall cases. This result should be anticipated from the modal contributions d_i, shown in Fig. 8, where only the first two modes contribute to the normal force calculation. Likewise, the quarter-chord pitching moment is well approximated for both cases, capturing the large nose down moment due to the dynamic stall vortex. The largest

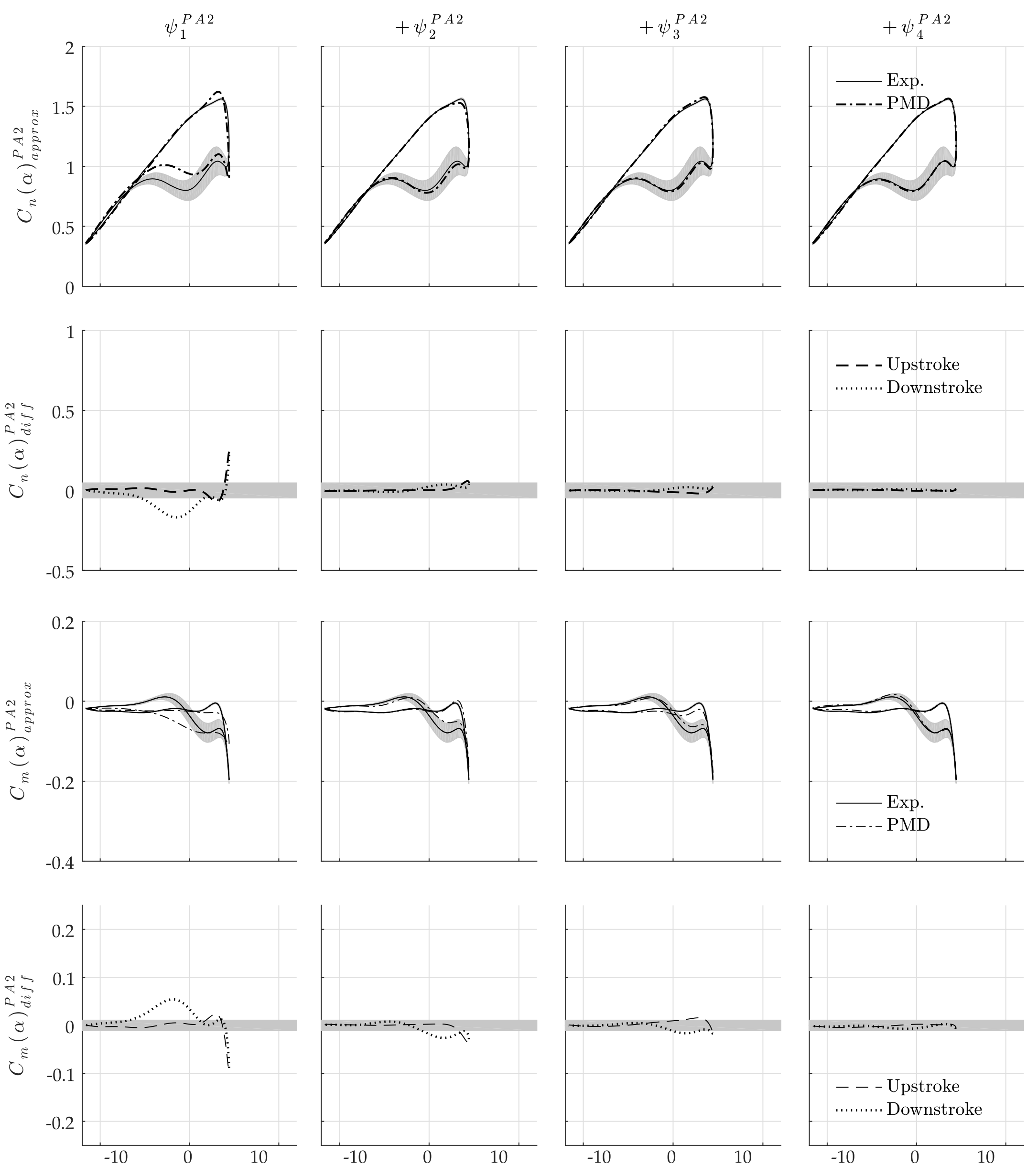

Fig. 10 PA2 light stall aerodynamic load reconstruction. Label definition in text. Approximation plots: phase-averaged experimental data (solid line), standard deviation (shaded area). Difference plots: ±5% maximum amplitude (shaded area).

discrepancies are seen to be on the upstroke near the top of the pitching trajectory for the deep stall case and case at the beginning of the downstroke motion for the light stall case. These two locations in the pitching trajectory both occur after the minimum quarter-chord pitching moment in the pitching trajectory. One way to interpret this result is that the final two modes, ψ_3 and ψ_4, serve to describe the airfoil surface pressure response to the ejection of the dynamic stall vortex into the wake. Adding these final two modes to the reconstructions demonstrates an exceptional approximation for both the normal force and quarter-chord pitching moment.

To quantify the efficiency of the four-mode reconstruction across the parameter space, the approximation error is calculated using the following metric:

$$\text{Error}_{\text{approx}} = \frac{1}{N_t}\left(\frac{\sum_{i=1}^{N_t}\beta_i}{C_x^*(k,\alpha_0)|_{\max} - C_x^*(k,\alpha_0)|_{\min}}\right)\times 100\% \tag{12}$$

where N_t is the number of time steps in the ensemble averaged trajectory, C_x^* is the load under consideration ($x = n, m$), and

$$\beta_i = \begin{cases} \left|C_x^*(t_i;k,\alpha_0) - \sum_{j=1}^{N_{\text{PMD}}} C^*_{\underset{\text{PMD}}{x,j}}(t_i;k,\alpha_0)\right| & \text{if } > \text{std}(C_x^*(t_i;k,\alpha_0)), \\ 0 & \text{if } <= \text{std}(C_x^*(t_i;k,\alpha_0)) \end{cases} \tag{13}$$

Here, N_{PMD} indicates the number of modes used for the approximation. The term β_i is simply the magnitude of the difference between the experimental data and the approximated result at the current ensemble averaged time stamp. However, if this difference is less that the experimental standard deviation at this time stamp, then β_i is set to 0, meaning that the approximation falls within the range of uncertainty of the experimental data. The resulting approximation error percentage is shown in Fig. 11 for both aerodynamic loads in all experimental cases. The abscissa for each subfigure is the collection of mean stall penetration angle of attack $\alpha_0 - \alpha_{ss}$ for the pitching cases. Likewise, the symbols within each plot differentiate the three different reduced frequencies k considered, i.e., $k = 0.020$ (crosses), $k = 0.050$ (open squares), and $k = 0.076$ (filled circles). Viewing the error percentage in this way shows the effect of reduced frequency and stall regime on the approximation.

It becomes immediately obvious that the normal force is very well approximated across the entire parameter space with only two modes ψ_1 and ψ_2. Using this two-mode approximation, the error is below 3% for all cases. Once again, the addition of ψ_3 and ψ_4 does not affect the normal force approximation significantly, partly due to the fact that the two-mode approximation represents the experimental data so well.

The approximation error behavior for the quarter-chord pitching moment is not immediately as intuitive. Using only the first mode ψ_1, the reduced frequency shows a minimal effect compared to the normal force one-mode approximation, whereas there is a distinct correlation with the mean angle of attack. Adding the second mode ψ_2 results in a dramatic decrease in error for nearly every case except for the lowest mean angles of attack, which correspond to attached flow pitching. Interestingly, the quasi-steady ($k = 0.020$) cases exhibit larger error than the unsteady cases with increasing magnitude as the mean angle of attack grows. With the exception of the $k = 0.076$, $\alpha_0 = 8$ deg case, every two-mode approximation has an error below 9%. Further reductions in error are realized with the introduction of ψ_3 and ψ_4, where the dependence on reduced frequency and mean angle of attack is nearly removed.

The general trend of larger error for the pitching moment coefficient at low stall penetration angles (i.e., $\alpha_0 - \alpha_{ss} < -5$ deg) was originally thought to be an artifact of the experimental weighting toward stalled configurations in the PMD ψ-mode calculation (see Table 3). To investigate the validity of this claim, PMD $\boldsymbol{\psi}$ modes were calculated using only the experimental configurations in each of the respective stall regimes: attached flow pitching (AF), light stall (LS), and deep stall (DS). The resulting ψ-mode shapes are shown in Fig. 12 where a correlation value comparing the mode shape to the PA2 $\boldsymbol{\psi}$ modes used thus far (indicated as "FULL") is calculated as

$$\eta = \int_{\Omega_x} \psi(\xi)^{\text{FULL}} \cdot \psi(\xi)^{(\#\#)}\,\mathrm{d}\xi, \qquad (\#\#) \in \{\text{AF, LS, DS}\} \tag{14}$$

The first two mode shapes for each subset calculation show good correlation with the FULL data set. However, the correlation of the higher-order modes significantly decreases for the attached flow pitching (AF) set, whereas the light stall (LS) and deep stall (DS) modes maintain a good correlation. The reduced qualitative behavior of the attached flow pitching subset higher-order modes (3 and 4) is most likely attributable to two causes: 1) a lack of data to smooth the behavior, or 2) a lack of coherent, repeatable structures in the flowfield resulting in a more dissociated mode shape. It is also interesting to note that, despite being well represented in the FULL

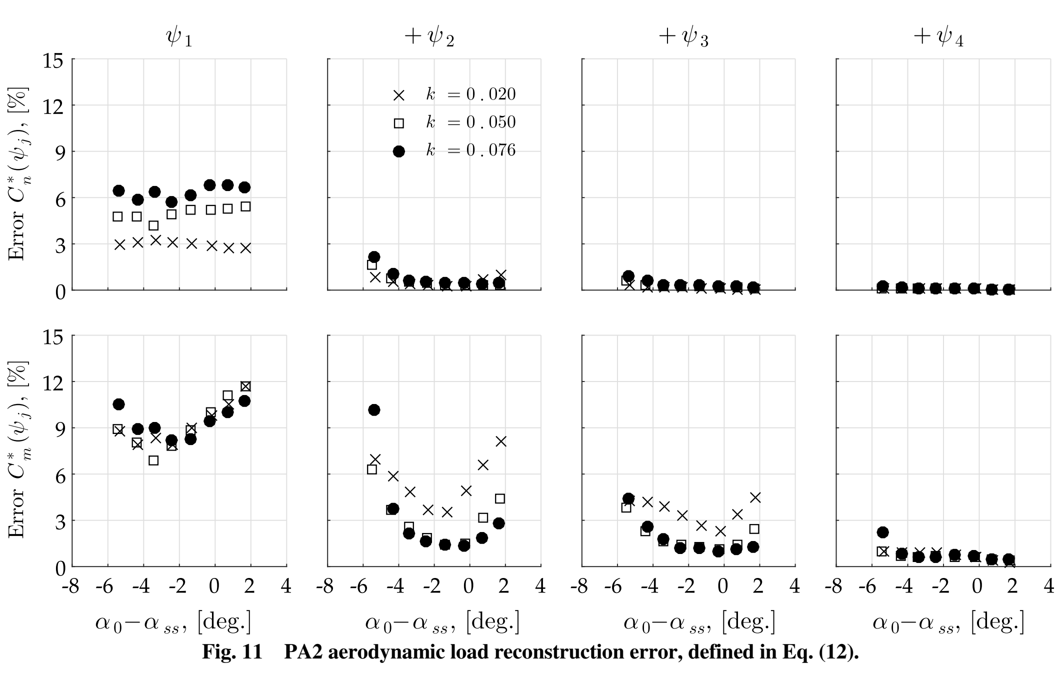

Fig. 11 PA2 aerodynamic load reconstruction error, defined in Eq. (12).

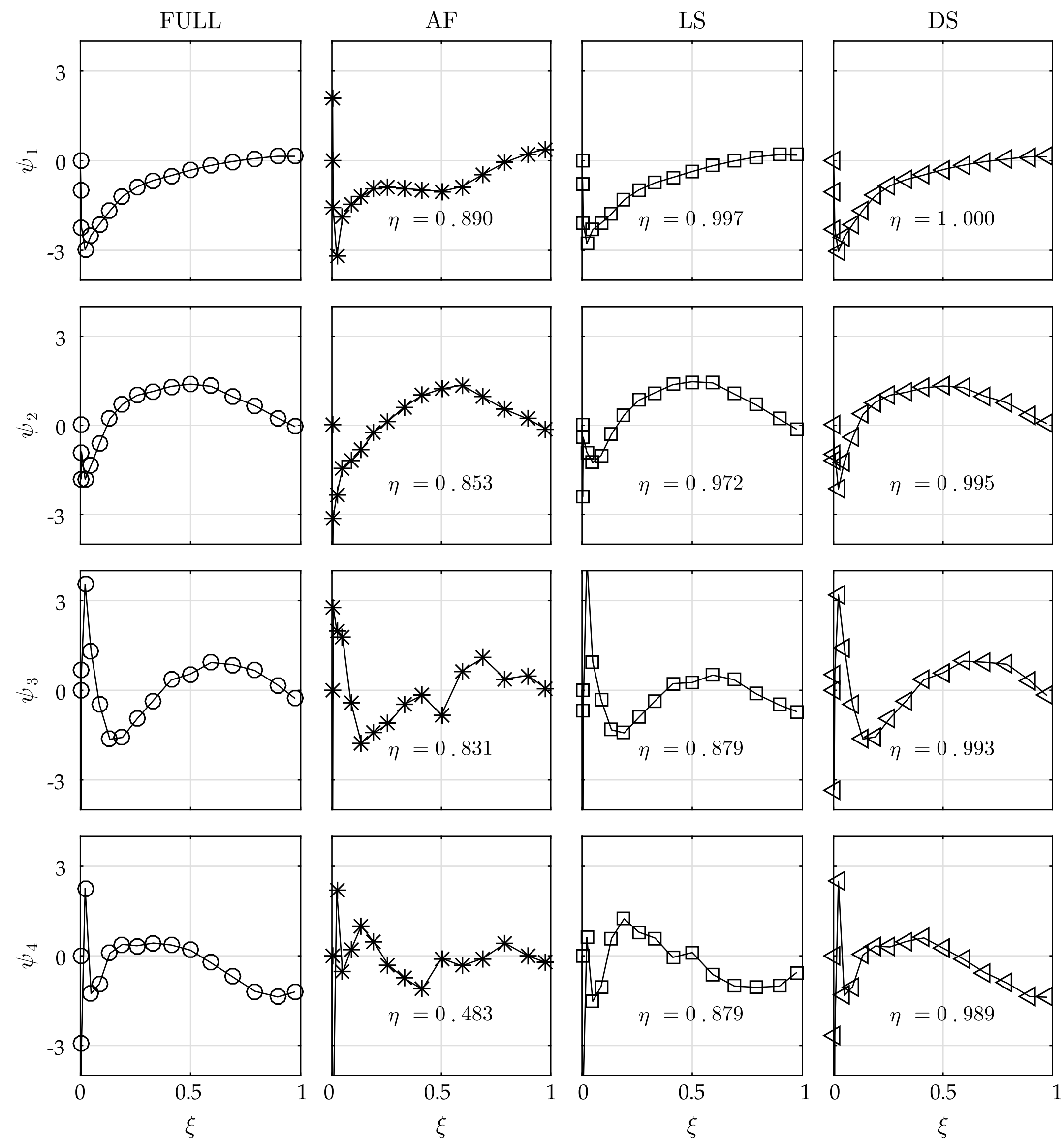

Fig. 12 PA2 ψ-mode shape comparison of basis calculated from subsets of the parameter space: full experimental set (FULL), attached flow basis (AF), light stall basis (LS), and deep stall basis (DS).

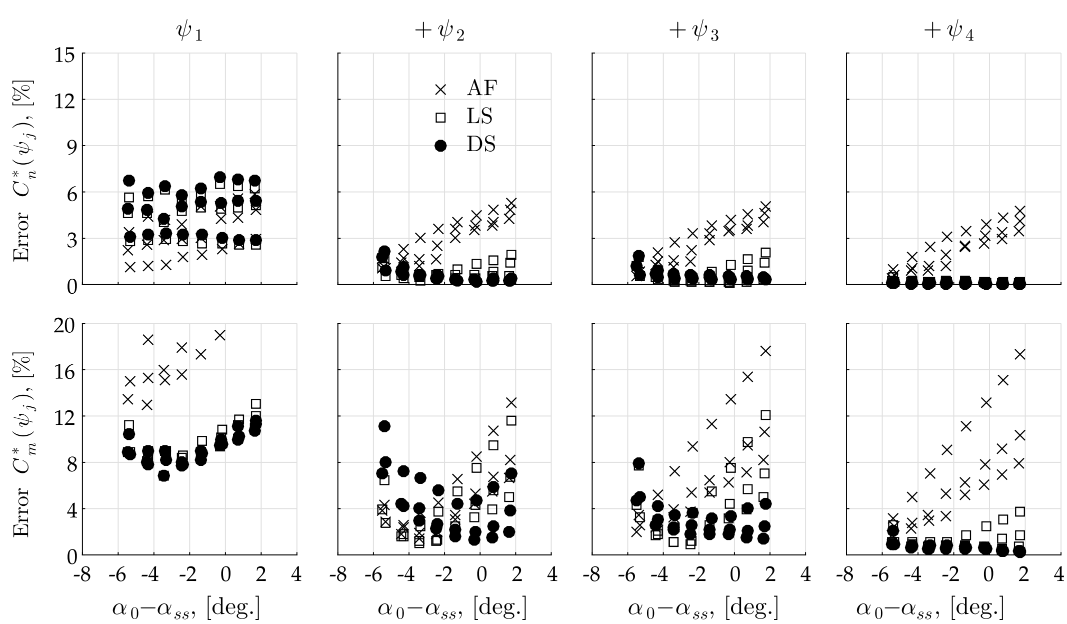

Fig. 13 PA2 aerodynamic load reconstruction error using ψ modes calculated from subsets of the parameter space: attached flow basis (AF), light stall basis (LS), and deep stall basis (DS).

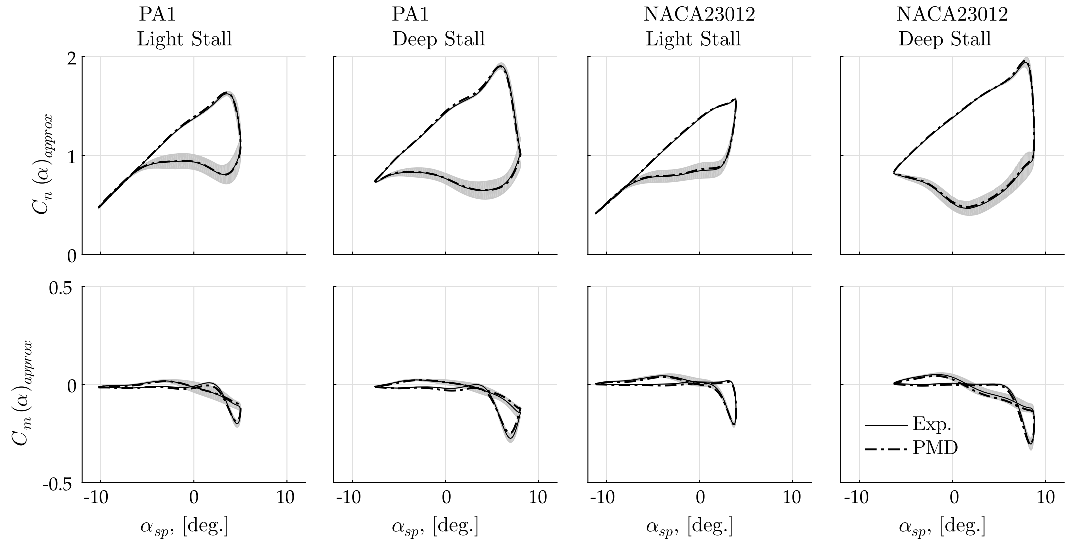

Fig. 14 Aerodynamic load reconstructions for the PA1 and NACA 23012 airfoils using the first four PA2 ψ modes. For label definitions, see the text.

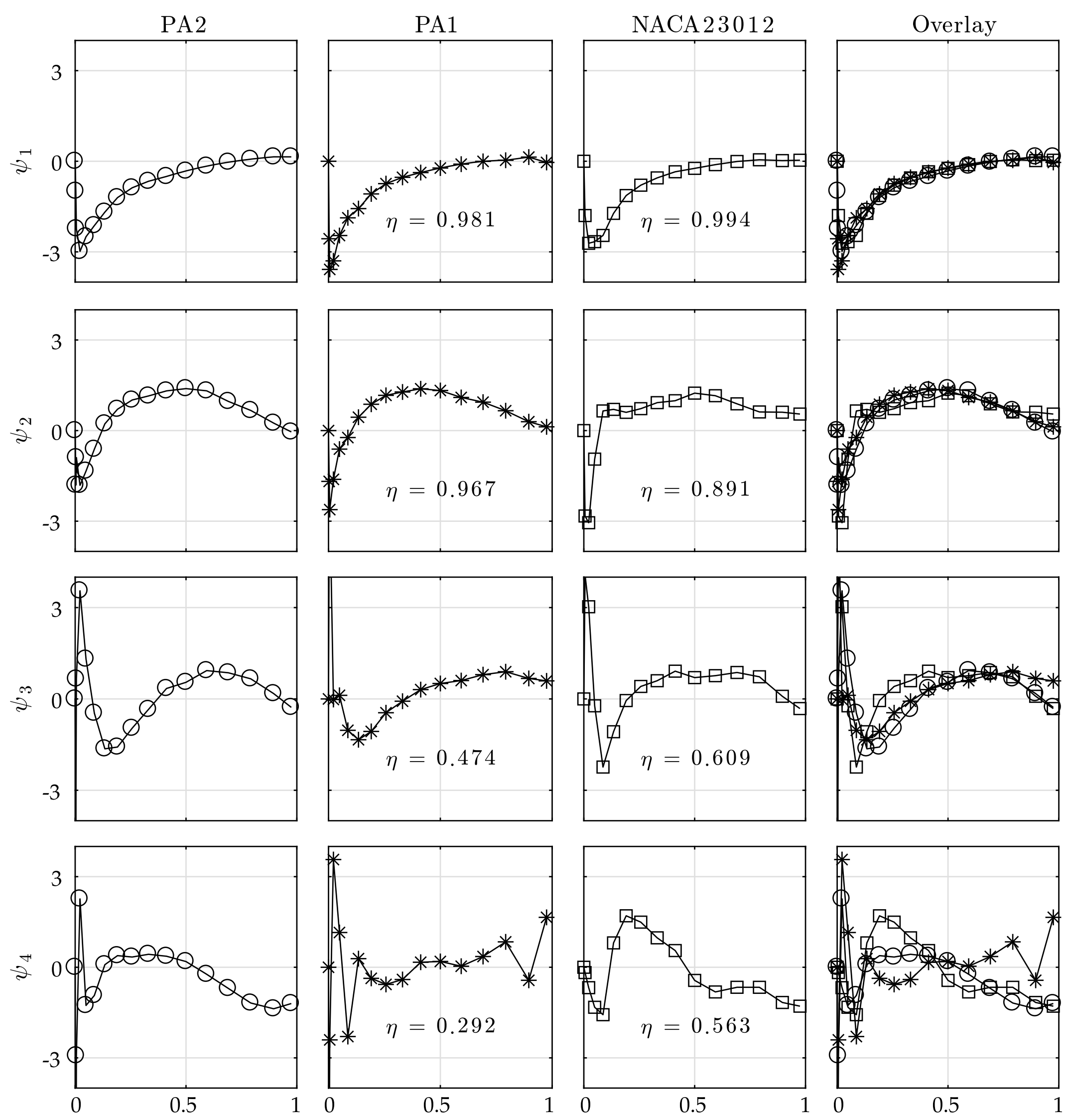

Fig. 15 ψ-mode comparison using different airfoil data sets.

data set calculation, the light stall (LS) mode shapes do not correlate as well as the deep stall (DS) mode shapes. In fact, the FULL PMD mode shape set could very well be calculated from only the deep stall data set without much change in the resulting reconstruction error.

Figure 13 shows the resulting parameter space reconstruction error for each subset ψ-mode calcuation (similar format to Fig. 11). As expected from inspection of the mode shapes, the ψ modes calculated from only the attached flow pitching (AF) subset do a poor job of reconstructing the light and deep stall normal force and quarter-chord pitching moment. However, notice that the four-mode reconstruction of the quarter-chord pitching moment error in the attached flow pitching regime ($\alpha_0 - \alpha_{ss} < -5$ deg) is no better than the deep stall reconstruction, indicating (at least for the amount of data available to calculate the AF ψ modes) that the error is not associated with parameter space weighting. The light stall (LS) ψ-mode calculation performs well in reconstructing the normal force throughout the parameter space; however, the quarter-chord pitching moment is not well constructed in the deep stall regime ($\alpha_0 - \alpha_{ss} > -1$ deg). Only the deep stall (DS) ψ-mode calculation reconstructs the entirety of the parameter space, for both the normal force and quarter-chord pitching moment, to the same level of fidelity as the FULL ψ-mode construction, which was to be expected from inspection of the correlation coefficients in Fig. 12.

D. ψ-Mode Reconstructions for Nonnative Geometries

The generic applicability of the derived ψ modes to describe dynamic stall for other airfoil geometries is investigated in this section. To do this, the pressure difference fields acquired from the PA1 and NACA 23012 airfoils are projected onto the PA2 ψ modes to evaluate the respective aerodynamic load reconstructions. Figure 14 shows the four-mode ($\psi_1^{\mathrm{PA2}}, \psi_2^{\mathrm{PA2}}, \psi_3^{\mathrm{PA2}}, \psi_4^{\mathrm{PA2}}$) aerodynamic load reconstructions for the PA1 and NACA 23012 airfoils in the light stall and deep stall environments as indicated. The first and second rows represent the normal force and quarter-chord pitching moment reconstructions, respectively. The abscissa of each subfigure is the stall penetration angle of attack α_{sp}. Perhaps somewhat unexpectedly, the reconstructions demonstrate a remarkable ability to represent the experimental data despite significant differences in the geometric parameters of the airfoil shapes (Table 1). It should also be noted here that the PA1 has a tripped leading-edge boundary layer similar to the PA2; however, the NACA 23012 results are for a natural transition behavior.

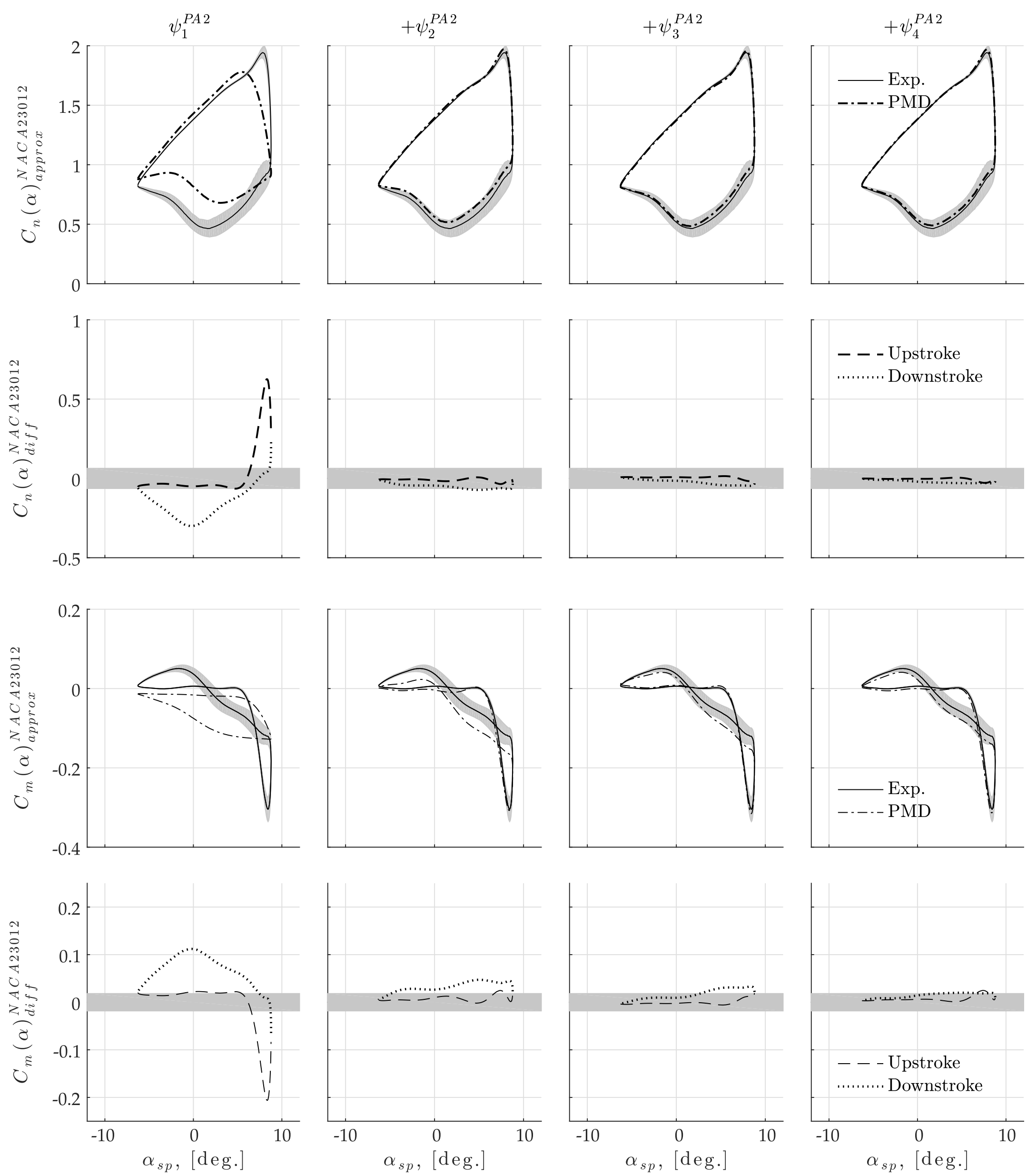

Fig. 16 NACA 23012 deep stall ($\alpha_0 = 15.7$ deg, $k = 0.104$) aerodynamic load reconstruction using the PA2 ψ modes.

The excellent reconstruction behavior of the PA1 and NACA 23012 aerodynamic loads using a nonnative ψ-mode set (PA2) suggests that the pressure difference field may have a similar structure with respect to PMD for the dynamic stall phenomenon regardless of the airfoil geometry.

Figure 15 shows a comparison of the first four ψ-mode shapes calculated for each airfoil geometry data set: PA2, PA1, and NACA 23012. As in Fig. 12, the η correlation value has been assigned using the PA2 ψ modes as reference. The final column of subfigures shows an overlay of the modes from each airfoil. Here, the first two modes in all cases show an excellent correlation indicating common features of the dynamic stall process for all the airfoil geometries. Mode 3 exhibits a qualitative similarity across the different geometries; however, the correlation value suggests a quantitative disagreement. It appears that the reduction in correlation is due to a disagreement in the chordwise location of the aft suction peak. PA2 has its peak around $\eta = 0.6$, whereas the peak for PA1 is around $\eta = 0.85$. In contrast, the NACA 23012 produces more of a suction pressure plateau, resulting in the lowest correlation value. The fourth mode shape is significantly different for each geometry, showing hardly any qualitative similarities. The dissimilar behavior of the fourth mode across the geometries is perhaps expected from the earlier PA2 analysis that suggested it may account for secondary flow structures, which may well be more geometry specific.

To further examine the modal reconstruction convergence with nonnative ψ modes, the NACA 23012 deep stall configuration ($\alpha_0 = 15.7$ deg, $k = 0.104$) in Fig. 16 is expanded in a format similar to the PA2 aerodynamic load reconstruction in Fig. 9. Because of the correlation of modes 1 and 2 across the geometries, it is observed that the normal force reconstruction maintains a rapid convergence regardless of the airfoil from which the ψ modes are calculated. Similarly, the quarter-chord pitching moment still exhibits a four-mode convergence, despite the fact that the fourth mode has little correlation between the geometries.

Finally, the PA2 deep stall case ($\alpha_0 = 13.9$ deg, $k = 0.078$) of Fig. 9 is reconstructed using the nonnative NACA 23012 ψ modes as shown in Fig. 17. As with the nonnative NACA 23012 reconstruction, the PA2 aerodynamic load reconstruction demonstrates a remarkable convergence, showing no significant discrepancies compared with the experimental data by the addition of the fourth mode. Although the normal force reconstruction shows some error on the downstroke with only two modes, the values all reside within the experimental standard deviation and provide an accurate representation of the aerodynamic behavior.

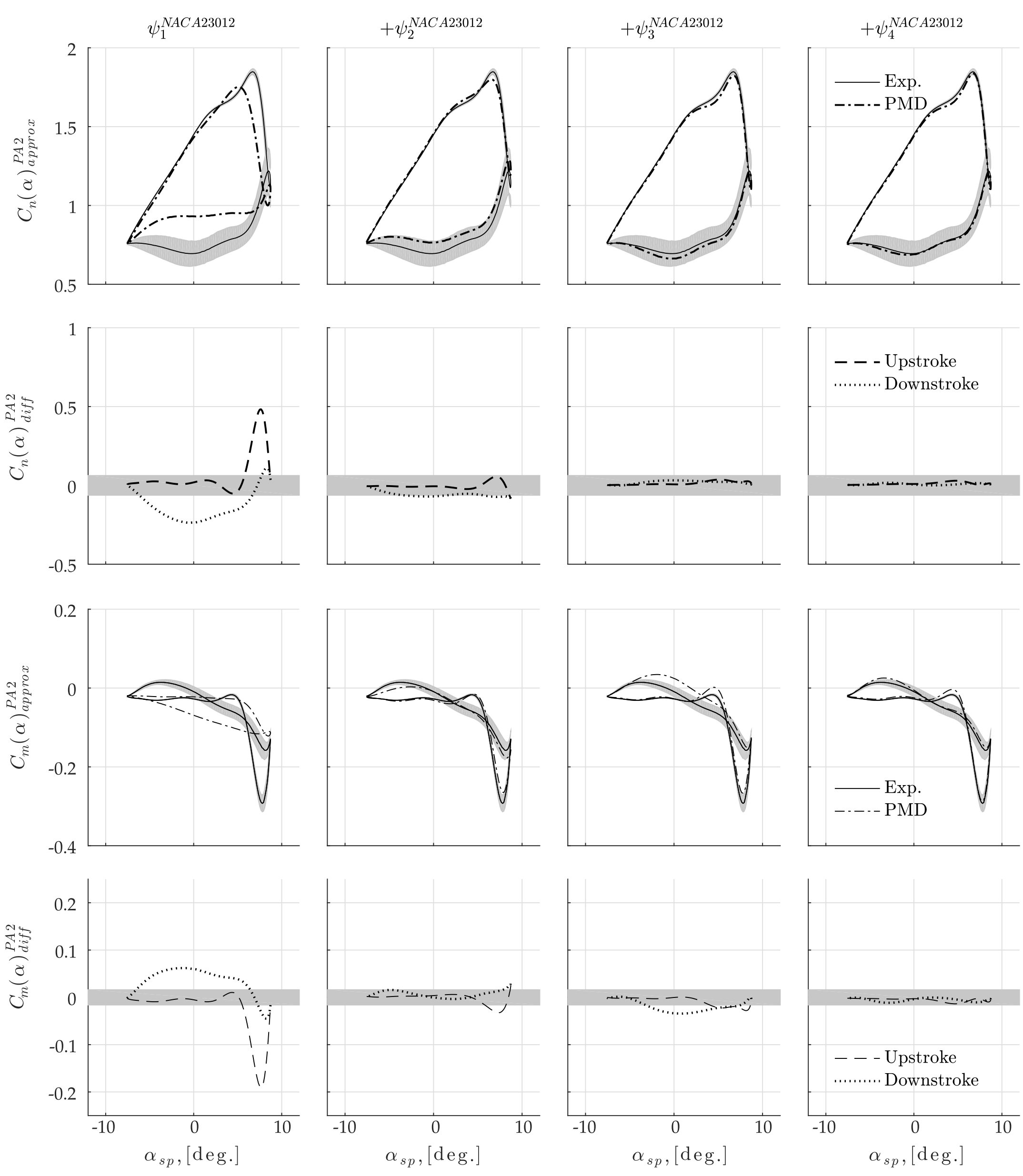

Fig. 17 PA2 deep stall ($\alpha_0 = 13.9$ deg, $k = 0.078$) aerodynamic load reconstruction using the NACA 23012 ψ modes.

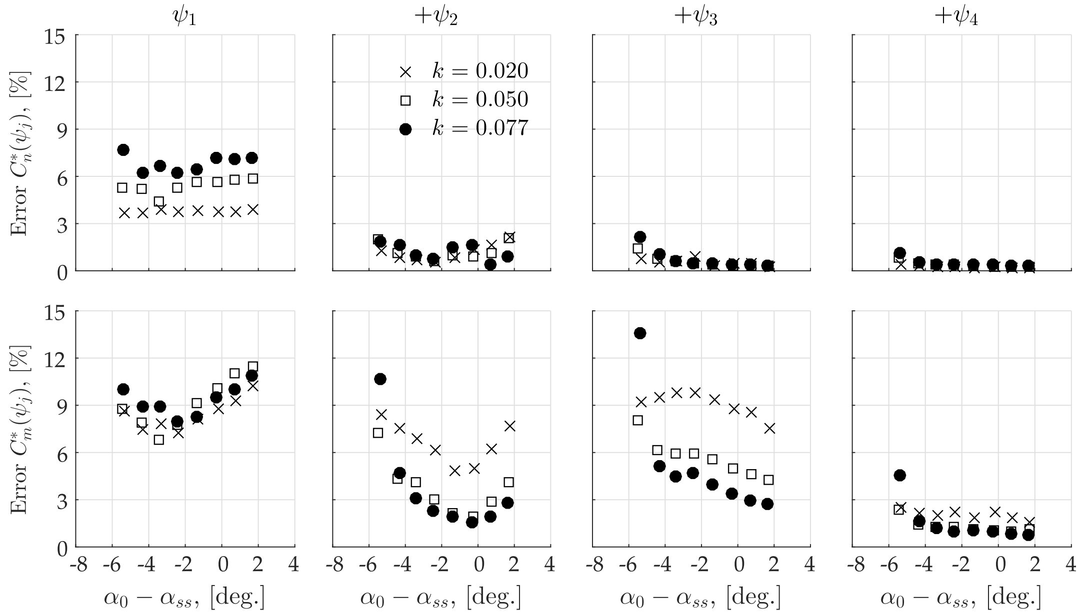

Fig. 18 PA2 aerodynamic load reconstruction error using ψ modes calculated from the NACA 23012 airfoil data set.

Figure 18 gives the PA2 reconstruction error across the entire parameter space using the nonnative NACA 23012 ψ modes. Remarkably, similar trends as gleaned from Fig. 11 for the native PA2 reconstruction are observed. In fact, the two-mode reconstruction is nearly identical in both trend and error magnitude. The largest discrepancy is the three-mode quarter-chord pitching moment reconstruction, in which the error actually increases in most cases compared to the two-mode reconstruction. The final four-mode reconstruction has a similar error magnitude for the normal mode reconstruction, whereas the quarter-chord pitching moment has only a slightly increased error magnitude compared to Fig. 11. The fourth mode addition demonstrates the robustness of the PMD technique where excellent reconstruction of both aerodynamic loads is still achieved across the parameter space despite the low correlation between ψ_4^{PA2} and $\psi_4^{\mathrm{NACA23012}}$.

V. Discussion

The parametric modal decomposition (PMD) presented herein has proven to be robust in the production of basis sets from which the dynamic stall phenomenon can be efficiently investigated. Key enabling procedures contributing to the observed efficiency of the modal aerodynamic load reconstructions include the following: 1) the change of reference frame from the unsteady, viscous pressure field to the unsteady perturbations around the calculated static attached flow pressure field; and 2) using the pressure difference field as opposed to the full surface pressure values. McCroskey [25] suggested that the pressure difference field would be more forgiving with respect to perturbations in the flowfield compared to the full surface pressure field, where in the currently investigated cases produced mode shapes that more or less correlated across the parameter space.

With these two procedures, the pressure difference field collection across a large range of operating conditions and airfoil geometries were decomposed using PMD to produce mode sets that provided optimal aerodynamic load and surface pressure field reconstruction throughout the parameter space. The extracted mode shapes were even able to reconstruct the pressure difference fields of nonnative airfoils (i.e., airfoils from which the mode shapes were not calculated).

Based on the results presented herein, it is conjectured that a two-mode approximation is sufficient for reconstructing the unsteady aerodynamic loads across all considered dynamic stall regimes regardless of the airfoil geometry. This conjecture requires further research for the modal structure of airfoils with varying static stall behavior. Namely, the three airfoils investigated in this study all exhibited leading-edge stall, whereas the modal behavior of trailing-edge stall airfoils is currently unknown. If true, this conjecture suggests that the dynamic stall phenomenon has a consistent structure with respect to the pressure difference field that is agnostic to the airfoil geometry. The presented parametric modal decomposition provides a low-order basis from which the dynamic stall phenomenon can be further investigated through the modal coefficients.

An additional recommendation for further investigation is to conduct a dynamical systems analysis of the modal coefficients across the parameter space for both native and non-native ψ-mode calcuations. Despite the pressure difference field being decomposed into a linear modal basis, the modal coefficients for forced oscillation inputs all exhibit nonlinear behavior when $|\dot{\alpha}| > 0$. Several nonlinear system modeling methods exist (e.g., Volterra series, particle filter methods for nonlinear state-space representations, Koopman analysis, etc.). These methods offer different lenses through which to view the modal dynamics. The primary concern of this dynamical system analysis is to define a way to establish the unsteady modal coefficients given static airfoil data and a pitching trajectory and to quantify the limits within which the parameters produce a valid reconstruction.

To support the physical interpretation of modes, it is suggested that conditional sampling (or the recently derived full-state estimation algorithm [16]) of time-resolved PIV of the external flowfield be implemented. This technique will elucidate relationships between the modal structure and nonlinear dynamics with corresponding flowfield structures. Identifying contributing flowfield parameters will also provide insight on the appropriate modeling techniques to be implemented to avoid "black-box" methods.

Acknowledgments

This work was funded by Bell Helicopter Textron and the Vertical Lift Consortium, formerly the Center for Rotorcraft Innovation and the National Rotorcraft Technology Center, U.S. Army Aviation and Missile Research, Development and Engineering Center under Technology Investment Agreement W911W6-06-2-0002, entitled National Rotorcraft Technology Center Research Program. This support is gratefully acknowledged.

References

[1] Corke, T. C., and Thomas, F. O., "Dynamic Stall in Pitching Airfoils: Aerodynamic Damping and Compressibility Effects," *Annual Review of Fluid Mechanics*, Vol. 47, 2015, pp. 479–505. doi:10.1146/annurev-fluid-010814-013632

[2] Ericsson, L. E., and Reding, J. P., "Unsteady Airfoil Stall," NASA TR-CR-66787, July 1969.

[3] Theodorsen, T., "General Theory of Aerodynamic Instability and the Mechanism of Flutter," NACA Rept. 496, 1935.
[4] Wagner, H., "Über die Entstehung des Dynamischen Auftriebes Von Tragflügeln," *Zeitschrift für Angewandte Mathematik und Mechanik*, Vol. 5, No. 1, 1925, pp. 17–35.
doi:10.1002/(ISSN)1521-4001.
[5] Von Kármán, T., and Sears, W. R., "Airfoil Theory for Non-Uniform Motion," *Journal of the Aeronautical Sciences*, Vol. 5, No. 10, 1938, pp. 379–390.
doi:10.2514/8.674
[6] Leishman, J. G., and Beddoes, T. S., "A Semi-Empirical Model for Dynamic Stall," *Journal of the American Helicopter Society*, Vol. 34, No. 3, 1989, pp. 3–17.
doi:10.4050/JAHS.34.3
[7] Petot, D., and Tran, C. T., "Semi-Empirical Model for the Dynamic Stall of Airfoils in View of the Application to the Calculation of Responses of a Helicopter in Forward Flight," *Vertica*, Vol. 5, 1981, pp. 35–53.
[8] Goman, M., and Khrabrov, A., "State-Space Representation of Aerodynamic Characteristics of an Aircraft at High Angles of Attack," *Journal of Aircraft*, Vol. 31, No. 5, 1994, pp. 1109–1115.
doi:10.2514/3.46618
[9] Williams, D. R., ReiBner, F., Greenblatt, D., Muller-Vahl, H., and Strangfeld, C., "Modeling Lift Hysteresis with a Modified Goman–Khrabrov Model on Pitching Airfoils," *45th AIAA Fluid Dynamics Conference*, AIAA Paper 2015-2631, 2015.
doi:10.2514/6.2015-2631
[10] Vieira, B. A. O., and Maughmer, M. D., "An Evaluation of Dynamic Stall Onset Prediction Methods for Rotorcraft Airfoil Design," *51st Aerospace Sciences Meeting*, AIAA Paper 2013-1093, Jan. 2013.
doi:10.2514/6.2013-1093
[11] Gordeyev, S., and Thomas, F. O., "A Temporal Proper Decomposition (TPOD) for Closed-Loop Flow Control," *Experiments in Fluids*, Vol. 54, No. 3, 2013, pp. 1–16.
doi:10.1007/s00348-013-1477-7
[12] Coleman, D. G., Thomas, F. O., Gordeyev, S., Heintz, K. C., and Corke, T. C., "Investigation of Incompressible Dynamic Stall Physics by Application of a Parametric Proper Orthogonal Decomposition," *53rd AIAA Aerospace Sciences Meeting*, AIAA Paper 2015-1068, 2015.
doi:10.2514/6.2015-1068
[13] Brunton, S. L., Proctor, J. L., and Kutz, J. N., "Discovering Governing Equations from Data By Sparse Identification of Nonlinear Dynamical Systems," *Proceedings of the National Academy of Sciences*, Vol. 113, No. 15, 2016, pp. 3932–3937.
doi:10.1073/pnas.1517384113.
[14] Brunton, S. L., Proctor, J. L., and Kutz, J. N., "Sparse Identification of Nonlinear Dynamics with Control (SINDYc)," *IFAC-PapersOnLine*, Vol. 49, No. 18, 2016, pp. 710–715.
doi:10.1016/j.ifacol.2016.10.249
[15] Brunton, S. L., Brunton, B. W., Proctor, J. L., Kaiser, E., and Kutz, J. N., "Chaos as an Intermittently Forced Linear System," *Nature Communications*, Vol. 8, No. 1, 2017.
doi:10.1038/s41467-017-00030-8
[16] Loiseau, J.-C., Noack, B. R., and Brunton, S. L., "Sparse Reduced-Order Modelling: Sensor-Based Dynamics to Full-State Estimation," *Journal of Fluid Mechanics*, Vol. 844, June 2018, pp. 459–490.
doi:10.1017/jfm.2018.147
[17] Holmes, P., Lumley, J. L., Berkooz, G., and Rowley, C. W., *Turbulence, Coherent Structures, Dynamical Systems and Symmetry*, Cambridge Univ. Press, Cambridge, United Kingdom, 1998.
[18] Mulleners, K., and Raffel, M., "The Onset of Dynamic Stall Revisited," *Experiments in fluids*, Vol. 52, No. 3, 2012, pp. 779–793.
doi:10.1007/s00348-011-1118-y
[19] Mulleners, K., and Raffel, M., "Dynamic Stall Development," *Experiments in fluids*, Vol. 54, No. 2, 2013, p. 1469.
doi:10.1007/s00348-013-1469-7
[20] Ramasamy, M., Wilson, J. S., McCroskey, W. J., and Martin, P. B., "Characterizing Cycle-to-Cycle Variations in Dynamic Stall Measurements," *Journal of the American Helicopter Society*, Vol. 63, No. 2, 2018, pp. 1–24.
doi:10.4050/JAHS.63.022002
[21] Jacobs, E. N., and Clay, W. C., "Characteristics of the N.A.C.A. 23012 Airfoil from Tests in the Full-Scale and Variable-Density Tunnels," NACA TR 530, 1935.
[22] Leishman, J. G., "Contributions to the Experimental Investigation and Analysis of Aerofoil Dynamic Stall," Ph.D. Thesis, Univ. of Glasgow, United Kingdom, 1984.
[23] Bowles, P., "Wind Tunnel Experiments on the Effect of Compressibility on the Attributes of Dynamic Stall," Ph.D. Thesis, Univ. of Notre Dame, Notre Dame, Indiana, Feb. 2012.
[24] Leishman, J. G., *Principles of Helicopter Aerodynamics*, Cambridge Univ. Press, Cambridge, United Kingdom, 2000.
[25] McCroskey, W. J., "Unsteady Airfoils," *Annual Review of Fluid Mechanics*, Vol. 14, 1982, pp. 285–311.
doi:10.1146/annurev.fl.14.010182.001441

C. W. Rowley
Associate Editor